J. Fluid Mech. (2013), vol. 732, pp. 316–331. © Cambridge University Press 2013
doi:10.1017/jfm.2013.409

Vorticity moments in four numerical simulations of the 3D Navier–Stokes equations

Diego A. Donzis[1], John D. Gibbon[2,†], Anupam Gupta[3], Robert M. Kerr[4], Rahul Pandit[3,5] and Dario Vincenzi[6]

[1]Department of Aerospace Engineering, Texas A&M University, College Station, Texas, TX 77840, USA

[2]Department of Mathematics, Imperial College London, London SW7 2AZ, UK

[3]Department of Physics, Indian Institute of Science, Bangalore 560 012, India

[4]Department of Mathematics, University of Warwick, Coventry CV4 7AL, UK

[5]Jawaharlal Nehru Centre for Advanced Scientific Research, Bangalore, India

[6]Univ. Nice Sophia Antipolis, CNRS, LJAD, UMR 7351, 06100 Nice, France

(Received 8 February 2013; revised 26 July 2013; accepted 3 August 2013)

The issue of intermittency in numerical solutions of the 3D Navier–Stokes equations on a periodic box $[0, L]^3$ is addressed through four sets of numerical simulations that calculate a new set of variables defined by $D_m(t) = (\varpi_0^{-1} \varOmega_m)^{\alpha_m}$ for $1 \leqslant m \leqslant \infty$ where $\alpha_m = 2m/(4m-3)$ and $[\varOmega_m(t)]^{2m} = L^{-3} \int_{\mathscr{V}} |\boldsymbol{\omega}|^{2m}\, \mathrm{d}V$ with $\varpi_0 = \nu L^{-2}$. All four simulations unexpectedly show that the D_m are ordered for $m = 1, \ldots, 9$ such that $D_{m+1} < D_m$. Moreover, the D_m squeeze together such that $D_{m+1}/D_m \nearrow 1$ as m increases. The values of D_1 lie far above the values of the rest of the D_m, giving rise to a suggestion that a depletion of nonlinearity is occurring which could be the cause of Navier–Stokes regularity. The first simulation is of very anisotropic decaying turbulence; the second and third are of decaying isotropic turbulence from random initial conditions and forced isotropic turbulence at fixed Grashof number respectively; the fourth is of very-high-Reynolds-number forced, stationary, isotropic turbulence at up to resolutions of 4096^3.

Key words: intermittency, isotropic turbulence, turbulence simulation

1. Introduction

1.1. *Background*

Intermittency in both the vorticity and strain fields is a dominant feature of developing and developed turbulence. It has been studied extensively both experimentally (Sreenivasan 1985; Meneveau & Sreenivasan 1991) and numerically (Kerr 1985; Jimenez *et al.* 1993; Donzis, Yeung & Sreenivasan 2008; Ishihara, Gotoh & Kaneda 2009; Donzis & Yeung 2010; Donzis, Sreenivasan & Yeung 2012; Yeung, Donzis & Sreenivasan 2012). Statistical physicists generally use velocity structure functions to study this phenomenon and have diagnosed the degree of intermittency by measuring how much the order-p velocity structure–function exponents ζ_p differ from a simple linear dependence on p (Frisch 1995; Schumacher, Sreenivasan & Yakhot 2007;

† Email address for correspondence: j.d.gibbon@ic.ac.uk

Boffetta, Mazzino & Vulpiani 2008; Pandit, Perlekar & Ray 2009). The standard way of quantifying equal-time, multiscaling exponents is a challenging experimental and numerical task (Arneodo *et al.* 2008; Ray, Mitra & Pandit 2008; Ray *et al.* 2011). The multiscaling approach is even more challenging for the three-dimensional (3D) Navier–Stokes equations

$$\partial_t \boldsymbol{u} + \boldsymbol{u}\cdot\nabla\boldsymbol{u} = \nu\Delta\boldsymbol{u} - \nabla P, \quad \operatorname{div}\boldsymbol{u} = 0, \tag{1.1}$$

because the velocity field $\boldsymbol{u}(\boldsymbol{x}, t)$ and pressure $P(\boldsymbol{x}, t)$ evolve in time, so, in general, time-dependent structure functions must be used to study dynamic multiscaling (Ray *et al.* 2008, 2011). In this paper, we introduce a way of analysing some new, and existing, numerical computations; our analysis gives new insights into, and provides a new method for distinguishing between, alternative regimes of behaviour in the vorticity field. To explain the nature of these regimes, let us consider the vorticity field $\boldsymbol{\omega} = \operatorname{curl}\boldsymbol{u}$ on a finite periodic domain $\mathscr{V} = [0, L]^3$ within the setting of the volume integrals which define a set of frequencies

$$\varOmega_m(t) = \left(L^{-3}\int_{\mathscr{V}} |\boldsymbol{\omega}|^{2m}\,\mathrm{d}V\right)^{1/2m}, \quad 1 \leqslant m \leqslant \infty. \tag{1.2}$$

Some recent work has centred around a dimensionless rescaling of the $\varOmega_m$ such that (Gibbon 2010, 2011, 2012, 2013)

$$D_m(t) = (\varpi_0^{-1}\varOmega_m)^{\alpha_m}, \quad \alpha_m = \frac{2m}{4m-3}, \tag{1.3}$$

where ϖ_0 is a fixed frequency defined by $\varpi_0 = \nu L^{-2}$. (For the forced Navier–Stokes equations, definition (1.2) must be modified by adding ϖ_0 to the integral term (Gibbon 2012).) The origin of the above rescaling, valid for both the Navier–Stokes and Euler equations, has been explained elsewhere (Gibbon 2011, 2012, 2013) where it has been shown that, with additive L^2-forcing, weak solutions obey the time average up to time T

$$\langle D_m\rangle_T \leqslant c\,Re^3 + O(T^{-1}). \tag{1.4}$$

The first in the hierarchy, $D_1 = \varpi_0^{-2}Z$, is proportional to the global enstrophy $Z = \varOmega_1^2$ and may be insensitive to deep fine-scale fluctuations. The higher D_m may be more sensitive so their measurement over a wide range of m could be a useful diagnostic of intermittency. However, the end of the sequence, $D_\infty(t)$, is hard to measure numerically, especially in highly intermittent flows. While Hölder's inequality enforces a natural ordering on the frequencies $\varOmega_m$ such that $\varOmega_m \leqslant \varOmega_{m+1}$ for $1 \leqslant m \leqslant \infty$, no such natural ordering is enforced on the D_m because the α_m *decrease* with m. Thus, there are two possible regimes:

$$D_{m+1}(t) < D_m(t) \quad \text{(regime I)}, \qquad D_m(t) \leqslant D_{m+1}(t) \quad \text{(regime II)}. \tag{1.5}$$

The issues to be addressed in this paper in our four numerical simulations of the 3D Navier–Stokes equations are as follows.

(*a*) Which of these regimes is favoured or is there an oscillation between them? If one regime is favoured, are the D_m well separated? What is the role of the enstrophy D_1?

(*b*) Are these orderings m-dependent?

(*c*) Are they Re-dependent?

(*d*) Are they dependent upon initial conditions?

1.2. *Simulations used for tests*

An important point with respect to numerical simulations of the weighted higher-order moments $D_m(t)$ is that their ratios might converge better than their actual values. This is consistent with the results reported in Donzis *et al.* (2008, 2012) and Yeung *et al.* (2012) where convergence for the ratios of higher-order vorticity and dissipation (strain) moments were obtained, even when the statistics of the individual moments showed no evidence of convergence (Kerr 2012). This answered a problem first raised in Kerr (1985) where it was noted that in forced simulations at modestly high Reynolds numbers, the averages of the vorticity and strain moments above sixth order did not converge. The determination of the $D_m(t)$ in simulations is not difficult whereas, in contrast, traditional numerical tools such as higher-order structure functions require a combination of larger domains and finer resolution than is currently feasible. In this paper, we calculate and compare the $D_m(t)$ from four data sets: two in which the average kinetic energy $E = L^{-3}\int_{\mathscr{V}} |\boldsymbol{u}|^2/2\,\mathrm{d}V$ decays in time and two in which E is held approximately constant by forcing at the low wavenumbers. The first is a unique data set from a computation in which fully developed turbulence forms from the interaction of two antiparallel vortices and whose kinetic energy E decays strongly after the first peak in the normalized enstrophy production $-S_u$ (Kerr 2013*a*). Some introductory discussion of this calculation is given in (§ 2). The other three data sets represent more traditional decaying and forced homogeneous, isotropic numerical turbulence. In the decaying calculations in § 2 and the decaying and forced calculations in § 3 the moments have been determined relatively continuously in time which makes a helpful comparison with the results of § 1. For the fourth data set (comprising resolutions up to 4096^3) of § 4, a similar conclusion is reached by studying the dependence of the time average of D_m on the Reynolds number. Inequality (1.4) is indeed uniform in m and, therefore, it is useful to study the behaviour of $\langle D_m\rangle_T$ for different m, although this does not provide information on the pointwise-in-time ordering of the D_m.

An advantage of the first data set described in § 2 is that the predicted convergence properties of ratios of the $D_m(t)$ can be tested for a calculation with huge fluctuations in the production of enstrophy, and therefore in the higher $D_m(t)$. That the calculation eventually exhibits traditional turbulent statistics and spectra is a bonus in justifying its use. However, this new initial condition is very specialized and any trends need to be confirmed using a more traditional decaying homogeneous, isotropic data set, which is the purpose of the second calculation discussed in § 3. Section 3 also contains forced simulations of homogeneous and isotropic turbulence at fixed Grashof number (a dimensionless measure of the ratio of the strength of the forcing term to that of the dissipative term; see, e.g., Doering & Gibbon (1995)). Finally, the fourth calculation in § 4 studies the time average of D_m from a forced, massively parallel, pseudo-spectral calculation (4096^3 with $Re_\lambda \approx 1000$) to show that these trends are not restricted to low or moderate Reynolds numbers.

Assessing the scaling of moments of intermittent quantities such as vorticity, strain rates or velocity gradients has been a critical component of characterizing and understanding intermittency. Of particular interest is how these moments scale with the Reynolds number, which is typically high in applications. At the same time, different orders provide information about fluctuations of different intensities. Low- and high-order moments, for example, are associated with weak and strong fluctuations. Thus, the understanding of the dependence of $\langle D_m\rangle_T$ on Re, especially at high m, can also shed light on the nature of intermittency and the most extreme events in turbulence.

1.3. *A summary of results*

The simulations described in §§ 2, 3 and 4, and illustrated in figures 2–4 and 7, each observe that a strict ordering occurs, as in regime I; namely $D_{m+1}(t) < D_m(t)$ in §§ 2 and 3 and $\langle D_{m+1}\rangle_T < \langle D_m\rangle_T$ in § 3 and in § 4 (on log-linear plots). To assess the significance of this, we write down the relation $D_{m+1} < D_m$ in terms of Ω_m and use Hölder's inequality $\Omega_m \leqslant \Omega_{m+1}$ on the extreme left-hand side

$$\varpi_0^{-1}\Omega_m \leqslant \varpi_0^{-1}\Omega_{m+1} < (\varpi_0^{-1}\Omega_m)^{\alpha_m/\alpha_{m+1}}. \tag{1.6}$$

As $m \to \infty$, $\alpha_m \searrow \alpha_{m+1}$, and so (1.6) shows that $\Omega_{m+1}/\Omega_m \searrow 1$. Thus, in regime I the Ω_m must be squeezed together for high m. In terms of the D_m, equation (1.6) is written as

$$D_m^{\alpha_{m+1}/\alpha_m} \leqslant D_{m+1} < D_m. \tag{1.7}$$

While respecting the ordering $D_{m+1} < D_m$, D_{m+1} is squeezed up close to D_m as $m \to \infty$

$$\lim_{m\to\infty} \frac{D_{m+1}}{D_m} \nearrow 1. \tag{1.8}$$

This squeezing phenomenon is observed in all four data sets where the D_m curves lie very close for $m > 3$ as in figures 2–4 and 7. Moreover, the values of D_1 in all four simulations lie far above the rest of the D_m giving rise to a suggestion, explored in § 5, that a depletion of nonlinearity is occurring which could be the cause of Navier–Stokes regularity. The most extreme intermittent events are represented by moments at increasingly large m. Our results suggest the saturation of these high-order moments. This is significant as it constrains the shape of the tails of the probability density function (p.d.f.) of vorticity which has been the focus of intense investigations (Kerr 1985; Jimenez *et al.* 1993; Donzis *et al.* 2008; Ishihara *et al.* 2009; Donzis & Yeung 2010; Donzis *et al.* 2012; Yeung *et al.* 2012). The fourth data set (forced, stationary, isotropic turbulence), the results of which are displayed in § 4, furnishes us with the opportunity to compare these results with other results on intermittency available in the literature. For example, within the multifractal model, Nelkin (1990) found that normalized moments of velocity gradients scale as

$$\langle u_x^p\rangle/\langle u_x^2\rangle^{p/2} \sim Re_\lambda{}^{d_p}, \tag{1.9}$$

where d_p is obtained from the multifractal spectrum and $\langle\cdot\rangle$ is the usual notation for the statistical average (see also Schumacher *et al.* 2007; Chakraborty, Frisch & Ray 2012). Using the well-known result $\langle u_x^2\rangle \sim (U_0/L)^2 Re_\lambda^2$ due to the dissipative anomaly, it is readily shown that $\langle u_x^p\rangle \sim Re_\lambda{}^{p+d_p}$. Our interest lies in the limit $p \to \infty$ where it can be shown that $\lim_{p\to\infty} d_p/p = c$. The constant c is given by $c = 3(1-\mathscr{D}_\infty)/(3+\mathscr{D}_\infty)$ with $\mathscr{D}_\infty$ representing the limit $\lim_{q\to\infty}\mathscr{D}_q$ of the generalized dimensions $\mathscr{D}_q$ (Hentschel & Procaccia 1983; Nelkin 1990). Clearly, moments of the form $\langle u_x^p\rangle^{1/p}$ saturate at high p, consistent with (1.8). Experimentally it is difficult to measure $\mathscr{D}_\infty$ reliably; its value appears to be smaller than 1.0 (Meneveau & Sreenivasan 1991). One can further show that the ratio of successive orders is

$$\langle u_x^{p+1}\rangle^{1/(p+1)}/\langle u_x^p\rangle^{1/p} \sim Re_\lambda^{(1+d_p/p)-(1+d_{p+1}/(p+1))}. \tag{1.10}$$

The limiting behaviour of d_p shows that $\lim_{p\to\infty}[(1+d_p/p)-(1+d_{p+1}/(p+1))] = 0$, and therefore the ratio on the left-hand side of (1.10) tends to a constant independent of p and Re_λ. Although data on the multifractal characteristics of vorticity are limited, measurements (Meneveau *et al.* 1990) suggest an asymptotic value $\mathscr{D}_\infty$ that is less

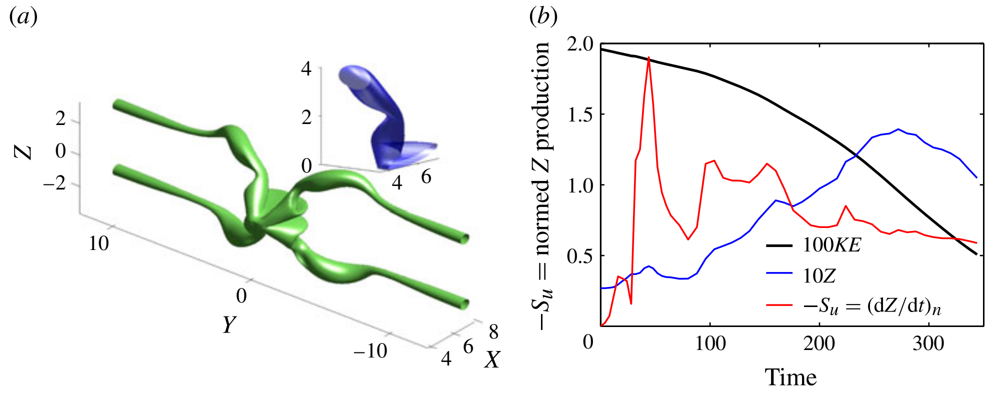

FIGURE 1. (Colour online) (*a*) Isosurfaces of the vorticity magnitude at $t = 16$, $|\omega| = 0.87$ and max $|\omega| = 8.7$. The initial condition is characterized by long antiparallel vortices with a localized perturbation for the $Re = 4000$ reconnection calculation. (*b*) Plots of the kinetic energy decay E, the enstrophy Z and its production, normalized to be consistent with experimental measurements of the velocity derivative skewness $-S_u$ (large y-domain with $\nu = 0.0005$). Here Z grows until $t \approx 270$ before falling, while E is always decaying.

than one, which is consistent with the unmistakable, but slow, squeezing together of Ω_m and D_m as m increases.

2. The first set of simulations

A recent Navier–Stokes vortex reconnection calculation (Kerr 2013*a*), with an early time shown in figure 1(*a*), has addressed the following long-standing numerical question: Can a Navier–Stokes initial condition with only a few vortices generate and sustain fully developed turbulence in a manner similar to how turbulence forms from the reconnection of antiparallel vortices in aircraft wakes, or from the reconnection of quantum vortex lines and rings (Kerr 2011)? This should include the formation of a high-wavenumber $k^{-5/3}$ kinetic energy spectrum and additional diagnostics indicating that the energy is cascading to small scales. Kerr (2013*a*) has shown that the spectrum and supporting diagnostics are consistent with those in homogeneous turbulent flows and has suggested that the cascade is formed by the creation of a chain of swirling vortex rings through the reconnection of the original three-dimensional vortex structures.

Kerr (2013*a*) achieved this goal by using a new initial condition that was designed to address the shortcomings, described in Bustamante & Kerr (2008), of the Kerr (1993) initial condition. The two most important properties of the new initial condition are: (i) their initial profiles and directions should be balanced in the sense that they are neither internally unstable nor prone to the shedding of waves or vortex sheet formation; (ii) their initial perturbations need to be localized far from the periodic boundaries, twice as far as in any previous antiparallel study. The calculation used an anisotropic mesh of $n_x \times n_y \times n_z = 512 \times 2048 \times 512$ in a $L_x \times L_y \times L_z = 2\pi(2 \times 8 \times 1)$ domain, with symmetries applied to the y and z directions. The evolved state at the time of the first reconnection is shown in figure 1(*a*).

In high-Reynolds-number experiments and numerical simulations, the appearance of a persistent $k^{-5/3}$ energy spectrum is commonly associated with the saturation of the normalized enstrophy production, which is usually written as the velocity

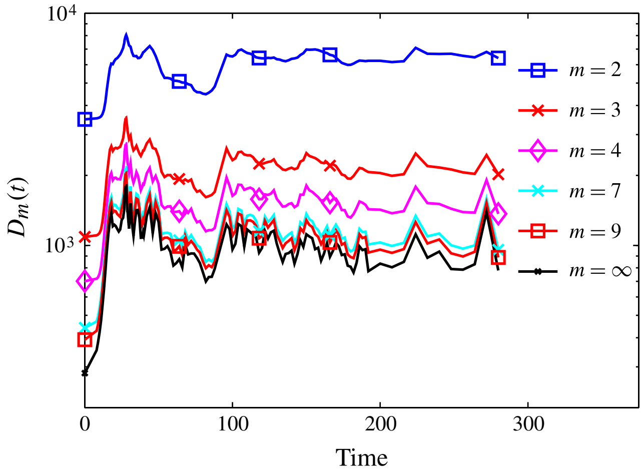

FIGURE 2. (Colour online) Curves of D_m ranging from $m = 2$ to $m = 9$ and including the normalized maximum of vorticity D_∞. The normalized enstrophy, D_1, is far above the log scale given here, so is omitted. The D_m are ordered for all values of *Re* and all times. Here $\nu = 0.0005$ and $L_x \times L_y \times L_z = 4\pi \times 16\pi \times 2\pi$.

derivative skewness $S_u = \langle u_x^3 \rangle / \langle u_x^2 \rangle^{3/2}$. Figure 1(*b*) shows a plot of $-S_u$ versus time for the reconnection calculation; likewise figure 3(*a*) shows the equivalent for the decaying isotropic calculation of § 3. The latest infinite *Re* estimates of S_u from forced turbulence calculations (Ishihara *et al.* 2009) have found $-S_u \approx 0.68$, consistent with experimental values of $-S_u \sim 0.5$–0.7. Early numerical calculations showed that the S_u tended to overshoot the early experimental values of $-S_u \approx 0.4$–0.5 before settling to the expected value (Orszag & Patterson 1972). Both figures 1(*b*) and 3(*b*) confirm this trend, with $-S_u$ rising above 0.6 before relaxing towards $-S_u \approx 0.6$.

In figure 2, note that all of the lower order D_m ($m = 1, \ldots, 9$) bound each higher-order D_m (on a logarithmic scale), for all times, mirroring the major fluctuations in $-S_u$. This can be expressed as $D_{m+1}(t) < D_m(t)$, thus favouring regime I as in (1.5). The enstrophy D_1 lies far above all of the other curves and has been omitted. Note the strong increase in the growth of each of the D_m, including D_∞, up until $t \approx 16$. This is the period when this calculation has nearly Euler dynamics and the effects of viscosity compared to nonlinear growth are minimal. The growth of the $D_m(t)$ in true Euler dynamics is the topic of another paper (Kerr 2013*b*).

3. The second and third sets of simulations: direct numerical simulation results for homogeneous, isotropic turbulence

Data from two direct numerical simulations (DNSs) of homogeneous, isotropic 3D Navier–Stokes turbulence are now presented. Both of these simulations use a pseudo-spectral method, a 2/3-rule for de-aliasing and 512^3 collocation points on a $[0, 2\pi]^3$ domain.

The first DNS is of decaying turbulence which reaches a Taylor-microscale Reynolds number $Re_\lambda \simeq 134$ at the main peak of the enstrophy Z associated with the formation of the inertial subrange. The Taylor-microscale λ is defined in the usual way in terms of the energy spectrum $E(k)$. The initial Fourier components of the

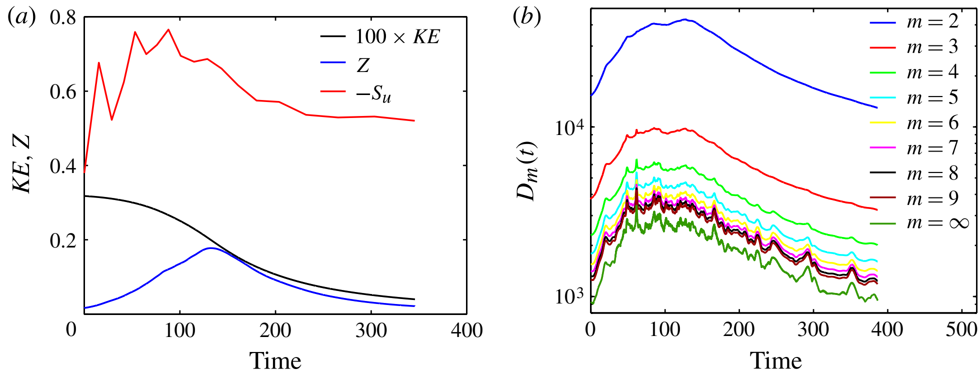

FIGURE 3. (Colour online) (*a*) A plot versus time t of the total kinetic energy (middle curve, shown in black online), the enstrophy Z (bottom curve, shown in blue online), the normalized enstrophy-production rate $-S_u$ (top curve, shown in red online) for our DNS of decaying, 3D Navier–Stokes isotropic turbulence. (*b*) A plot of the $D_m(t)$ for $2 \leqslant m \leqslant 9$ (top (blue online) to second from bottom (brown online) curves) and $D_\infty(t)$ (bottom (dark green) curve) for decaying isotropic turbulence; the value of D_1 is very high, so it is omitted. Zooming in on (*b*) makes it clear that $D_{m+1}(t) < D_m(t)$ for all values of m considered and for all t.

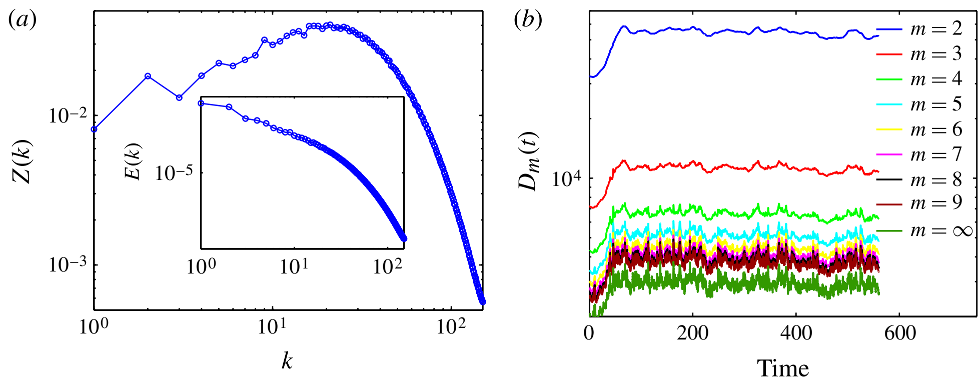

FIGURE 4. (Colour online) (*a*) The enstrophy spectrum for statistically steady forced turbulence at $Gr = 4.9 \times 10^7$. The inset shows the kinetic-energy spectrum for the same simulation. (*b*) The time series of $D_m(t)$ for statistically steady forced turbulence at $Gr = 4.9 \times 10^7$ $(m = 1, \ldots, 9)$. Zooming in on the right figure makes it clear that $D_{m+1}(t) < D_m(t)$ for all values of m considered and for all t.

velocity $\tilde{\boldsymbol{u}}_0(\boldsymbol{k})$ for the wave-vector $k = |\boldsymbol{k}|$ are generated by applying random phases to the energy spectrum $E_0(k) = E_0 k^4 \exp\{-2k^2\}$. The kinematic viscosity is $\nu = 5 \times 10^{-5}$.

The second DNS is a study of statistically steady turbulence which attains $Re_\lambda \simeq 182$; the forcing term $\boldsymbol{f}_u(\boldsymbol{x}, t)$ is specified most simply in terms of $\tilde{\boldsymbol{f}}_u(\boldsymbol{k}, t)$ whose spatial Fourier components are

$$\tilde{\boldsymbol{f}}_u(\boldsymbol{k}, t) = \frac{\mathscr{P}\Theta(k_f - k)}{\sqrt{2E_u(k_f, t)}}\boldsymbol{u}(\boldsymbol{k}, t), \quad E_u(k_f, t) = \sum_{k \leqslant k_f} E(\boldsymbol{k}, t), \tag{3.1}$$

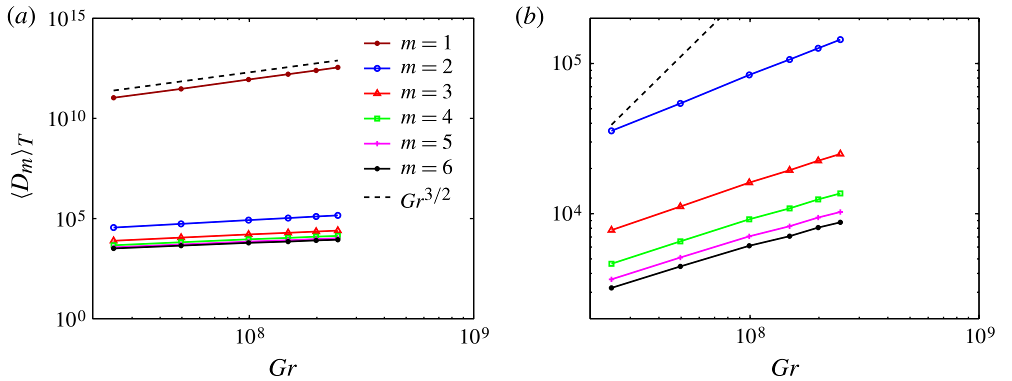

FIGURE 5. (Colour online) (*a*) Average values of D_m as a function of Gr for statistically steady forced turbulence at fixed Grashof number ($m = 1, \ldots, 6$). The dashed black line is $Gr^{3/2}$. The plot in (*b*) is the same as (*a*) but on a different vertical scale with $m = 2, \ldots, 6$.

where Θ is the Heaviside function and $k_f = 2$ is the wavenumber above which Fourier modes are not forced. This forcing term maintains a constant Grashof number $Gr = L^3 \mathscr{P}/\nu^2$ with $L = 2\pi$: for a similar forcing term that holds the energy injection fixed see Sahoo, Perlekar & Pandit (2011). The Grashof number is varied between 2.48×10^7 and 2.48×10^8 by changing $\mathscr{P}$ while keeping $\nu = 10^{-4}$ constant.

For the decaying DNS, a small inertial subrange forms at $t = 100$ when the enstrophy Z reaches its main peak. Assuming $E(k) = K_0(k)\epsilon k^{-5/3}$, the prefactor $K_0(k)$ is roughly 1.5 for about half a decade of wavenumbers. Similar to figure 1(*b*), 3(*a*) shows the time dependence of the kinetic energy E, enstrophy Z and its skewness $-S_u$. For the forced DNS at $Gr = 4.9 \times 10^7$, the energy and enstrophy spectra, in the statistically steady state, are given in figure 4(*a*). These spectra show that high-wavenumber fluctuations of both the velocity and vorticity fields are well resolved in our simulation; the same holds for the other values of Gr considered.

Figures 3(*b*) and 4(*b*) show $D_m(t)$ versus time t for $m = 2, \ldots, 9$ and $D_\infty = (\varpi_0^{-1}\|\omega\|_\infty)^{\alpha_\infty}$ with $\alpha_\infty = 1/2$ for both the decaying and forced DNS calculations, respectively. These plots show that $D_m(t) < D_{m+1}(t)$ for all t and thus support the generality of figure 2 of § 2.

The average values of D_m, as a function of Gr, are given in figure 5 for $m = 1, \ldots, 6$. The behaviour of $\langle D_m \rangle_T$ is consistent with the uniform bound $\langle D_m \rangle_T \leqslant c_1 Gr^{3/2}$, which can be obtained by combining (1.4) (Gibbon 2011) with the saturation of the bound $Gr \leqslant c_2 Re^2$ (Doering & Foias 2002). Moreover, the average values of D_m satisfy $\langle D_{m+1} \rangle_T < \langle D_m \rangle_T$ for all m and Gr considered, which is consistent with regime I.

A remark on the calculation of D_m concludes this section. Here $D_m(t)$ is defined from the space integral of the $2m$th power of $\boldsymbol{\omega}$ at time t. To compute $D_m(t)$, a sufficiently fine grid is required, especially if m is large. In our DNSs, the number of collocation points is 512^3. The energy and enstrophy spectra given in figure 4(*a*) already show that small-scale fluctuations are sufficiently well resolved. However, to confirm that the resolution is sufficient, we have computed $D_m(t)$ on a coarser grid by using only N^3 of the 512^3 available grid points with $N = 256, 128$. We have repeated this calculation for some illustrative values of t. Our results show that the values of D_m (even for $m = 9$) are reliable up to four or five significant figures. The difference

N^3	D_1	D_2	D_3	D_4	D_5	D_6	D_7	D_8	D_9	D_∞
512^3	2.9268×10^{11}	54065.5	11088.3	6407.7	4924.3	4238.3	3853.4	3610.9	3445.7	2719.4
256^3	2.9267×10^{11}	54062.8	11085.8	6404.7	4921.4	4235.9	3852.0	3610.4	3446.0	2623.3
128^3	2.9288×10^{11}	54123.7	11149.7	6502.0	5045.7	4374.3	3994.4	3750.9	3581.5	2482.0

TABLE 1. Forced DNS at $Gr = 4.9 \times 10^7$: values of the D_m at $t = 621$ (i.e. at the end of the simulation) calculated by using different numbers N^3 of grid points.

N^3	D_1	D_2	D_3	D_4	D_5	D_6	D_7	D_8	D_9	D_∞
512^3	2.7714×10^{10}	24663.7	6138.6	3860.5	3122.4	2779.3	2586.3	2464.2	2381.7	1980.4
256^3	2.7715×10^{10}	25667.9	6141.1	3862.4	3122.8	2777.2	2581.1	2456.0	2369.8	1980.4
128^3	2.7683×10^{10}	24621.0	6103.0	3807.0	3051.0	2694.3	2491.0	2360.7	2270.5	1705.8

TABLE 2. Decaying DNS: values of the D_m at $t = 128$ (i.e. at the peak of the enstrophy) calculated by using different numbers N^3 of grid points.

between D_1 and D_9 appear at the level of the second significant figure. Thus, we conclude that $D_{m+1}(t) < D_m(t)$ for all of the values of m and t we have considered. Representative examples are given in tables 1 and 2. It is possible to infer from these tables that the calculation of D_m for much greater m would require an even higher resolution. Finally, in the calculation of $\langle D_m \rangle_T$, we have checked the convergence of the time average for all the m shown in figure 5 ($m = 1, \ldots, 6$).

4. The fourth set of simulations: forced stationary isotropic turbulence

The DNS data in this fourth set of simulations were obtained using a massively parallel pseudo-spectral code which achieves excellent performance on $O(10^5)$ processors. The basic numerical scheme is that of Rogallo (1981). The time stepping is second-order Runge–Kutta and the viscous term is exactly treated via an integrating factor. Aliasing errors are carefully controlled by a combination of truncation and phase-shifting techniques. The database includes simulations with resolutions up to 4096^3 and Taylor–Reynolds number up to $Re_\lambda \approx 1000$ (see Donzis *et al.* 2012; Yeung *et al.* 2012). In order to maintain a stationary state, turbulence is forced numerically at the large scales. Since our objective here is to assess the generality of the ordering of the moments D_m, we show results using the stochastic forcing of Eswaran & Pope (1988) (denoted as EP) as well as a deterministic scheme described in Donzis & Yeung (2010) (denoted as FEK). In essence, this keeps the energy in the lowest wavenumbers fixed. For these two forcing schemes, the wavenumbers affected by forcing are confined to within a sphere $k < k_F$, where k_F is of order two or three. In order to capture intense events, which are the main contributors to high-order moments, resolution issues have to be properly addressed. Motivated by the theoretical work of Yakhot & Sreenivasan (2004), resolution effects have been studied in Donzis *et al.* (2008) and Yeung *et al.* (2012) with the conclusion that although high-order moments may be under-predicted using the standard resolution criterion, typically in simulations aimed at pushing up the Reynolds number, *ratios* of high-order moments are weakly affected by resolution issues. Small-scale resolution for a spectral simulation is typically quantified with the parameter $k_{max}\eta$ where $k_{max} = \sqrt{2}N/3$ is the highest resolvable wavenumber in a domain of size $(2\pi)^3$ with N^3 grid points. Simulations aimed at pushing the Reynolds number have typically used $k_{max}\eta$ between 1 and 2. Here we present results from $k_{max}\eta$ from the standard 1.5 up to 11, when available, which allows us to assess the effect of insufficient resolution. Table 3 summarizes those parameters of the DNS database that have been used.

4.1. *The D_m moments in forced stationary isotropic turbulence*

The time average of even moments of vorticity, $\langle \Omega_m \rangle_T$, are shown in figure 6. As assured by Hölder's inequality it can be seen that $\langle \Omega_{m+1} \rangle_T > \langle \Omega_m \rangle_T$ at all Reynolds numbers. Figure 6 also shows the line $\sim Re_\lambda$ (dashed), which is the result of the dissipative anomaly. This is easily obtained from the kinematic relation $\langle \epsilon \rangle = \nu \langle \Omega_1^2 \rangle_T$ associated with isotropic turbulence and the well-known scaling $\langle \epsilon \rangle \sim U_0^3/L$. It can then be shown that $\langle \Omega_1 \rangle_T \sim (U_0/L)Re^{1/2} \sim (U_0/L)Re_\lambda$, where the well-known result $Re_\lambda^2 \sim Re$ has been used. The DNS data in figure 6 agree with this scaling. As mentioned above, some resolution effects can be expected especially for high orders. Where data at nominally the same Reynolds number but different resolution is available, moments tend to be higher for higher values of $k_{max}\eta$ (see Donzis *et al.* 2008). This is clearer at higher Reynolds number ($Re_\lambda \approx 650$ where two resolutions are available). Ratios of moments, however, are only weakly affected by resolution,

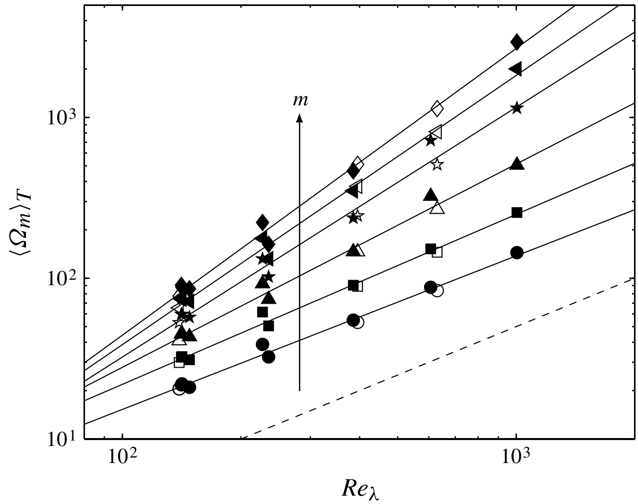

FIGURE 6. Scaling of $\langle \Omega_m \rangle_T$ as a function of Re_λ for forced stationary isotropic turbulence with resolutions up to 4096^3. Lines are for $m = 1$ (circles), $m = 2$ (squares), $m = 3$ (triangles), $m = 4$ (stars), $m = 5$ (left triangles) and $m = 6$ (diamonds). Open and closed symbols correspond to EP and FEK forcing, respectively. Dashed line is $\sim Re_\lambda^6$ (see the text). Note that for $Re_\lambda \approx 650$ at 4096^3 with FEK forcing, moments up to fourth order (instead of sixth) are available from our database.

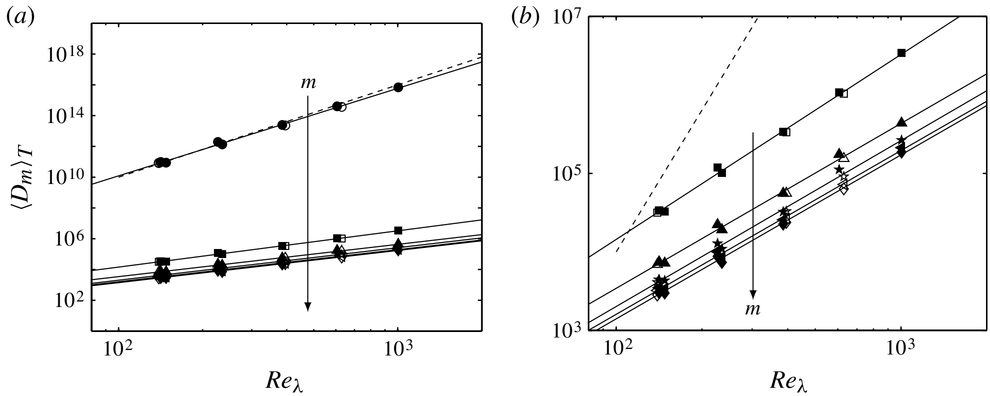

FIGURE 7. Scaling of $\langle D_m \rangle_T$ and ratios as a function of Re_λ for forced stationary isotropic turbulence with resolutions up to 4096^3: (*a*) D_m versus Re_λ for $m = 1$–6, while (*b*) is a zoom of (*a*) to highlight the ordering of $\langle D_m \rangle_T$ for $m = 2$–6. In both parts the dashed lines correspond to Re_λ^6.

which is also consistent with more recent results (Donzis *et al.* 2008, 2012; Yeung *et al.* 2012). In figure 7, the time averages $\langle D_m \rangle_T$ are shown as a function of Re_λ. For $m = 1$, one can again resort to using the dissipative anomaly with the definition $D_1 = (\varpi_0^{-1} \Omega_1)^2$. The result is

$$\langle D_1 \rangle_T = (L^2 \sqrt{\langle \epsilon \rangle} / \nu^{3/2})^2 \sim Re^3 \sim Re_\lambda^6 \tag{4.1}$$

N	Re_λ	$k_{max}\eta$	Forcing
256	140	1.4	EP
256	140	1.4	FEK
512	140	2.7	FEK
2048	140	11.2	FEK
512	240	1.4	FEK
2048	240	5.1	FEK
1024	400	1.4	FEK
2048	400	2.8	EP
2048	650	1.4	EP
4096	650	2.7	FEK
4096	1000	1.3	FEK

TABLE 3. Parameters of statistically stationary forced simulations: included are the resolution N, Re_λ, the resolution parameter $k_{max}\eta$ and the forcing type (see the text).

which is seen in figure 7(*a*). To see further details of higher-order moments figure 7(*b*) does not include $\langle D_1\rangle_T$. As in §§ 2 and 3, the data clearly shows the ordering $\langle D_{m+1}\rangle_T < \langle D_m\rangle_T$. The insensitivity of the time averages of the moments to the type of forcing and the much weaker effect of resolution compared with $\langle \Omega_m\rangle_T$ in figure 6 is also noted. The data also suggest that the ratio between the time averages of successive moments decreases with m, which is consistent with the asymptotic behaviour of (1.8). This is seen more clearly in figure 8, where the ratio of the time averages of successive moments, $\langle D_{m+1}\rangle_T/\langle D_m\rangle_T$, is plotted for different values of m. Consistent with an ordering $\langle D_{m+1}\rangle_T < \langle D_m\rangle_T$, the ratio is always less than unity. As m increases, however, this ratio becomes increasingly closer to unity in agreement with (1.8). It is also interesting that these ratios appear to be independent of Reynolds numbers which suggest a regime I ordering with clustering of moments at high m also in the high-Re_λ limit. Resolution effects, while weak, can still be seen upon careful examination of the data, especially at high orders. However, for a given simulation, the ordering of regime I is unchanged with resolution.

5. Concluding remarks: the depletion of nonlinearity

The recent introduction of the D_m vorticity moment scaling (Gibbon 2011, 2012, 2013) motivated by the time average (1.4), has suggested that they should be applied to independent numerical simulations, such as the four data sets here. All four unexpectedly show that the D_m obey the ordering of regime I, namely $D_{m+1} < D_m$, which leads to the squeezing effect of (1.8) such that $\Omega_{m+1}/\Omega_m \searrow 1$ and $D_{m+1}/D_m \nearrow 1$ as m increases. This has an effect on the shapes of the p.d.f. tails, as remarked in § 1.3. The ordering in the D_m is strict, even during intense events and, for $m \geqslant 3, 4$, the plots almost touch while replicating each other's shape, as in figures 2, 3(*b*), 4(*b*) and 7(*b*). It might be asked whether this is a viscous effect, a strictly nonlinear effect, or the result of some surprising symbiosis between the two? Using a variation of the antiparallel initial condition used in § 2, new Euler calculations have repeated this ordering over an extended period (Kerr 2013*b*), which implicates the nonlinear terms as the primary source. However, there is neither evidence from Navier–Stokes analysis

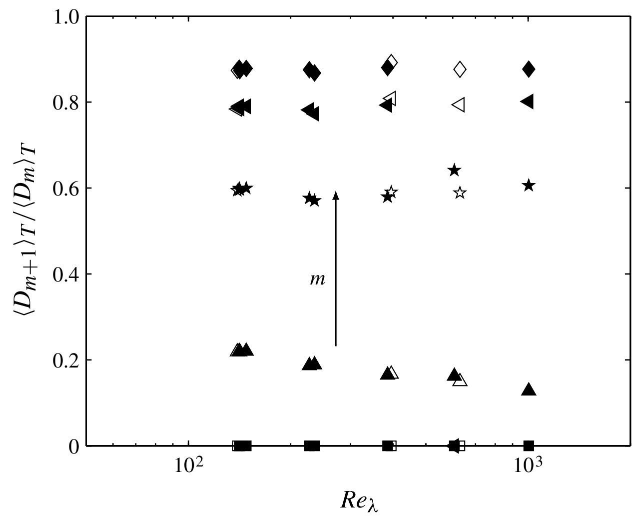

FIGURE 8. Ratio of moments $\langle D_{m+1}\rangle_T/\langle D_m\rangle_T$ for $m=1$ (squares), $m=2$ (triangles), $m=3$ (stars), $m=4$ (left triangles) and $m=5$ (rhombi) as a function of Re_λ.

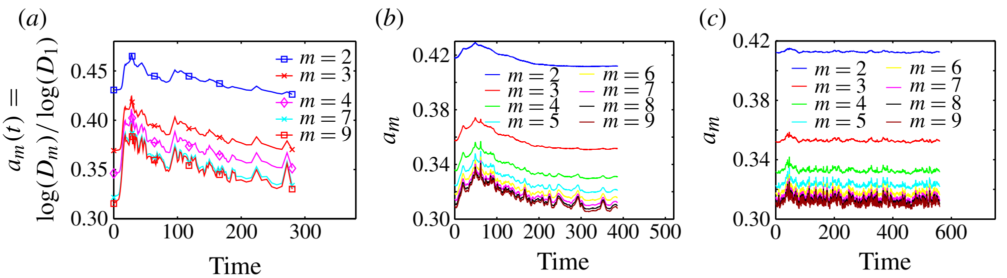

FIGURE 9. (Colour online) Plots of a_m for the three simulations in §§ 2 and 3 in which $a_m < 1/2$: (*a*) for the calculation in § 2 ($\nu = 0.0005$, $L_x \times L_y \times L_z = 4\pi \times 16\pi \times 2\pi$) and (*b*,*c*) for the decaying and forced calculations in § 3.

that such an ordering should hold, nor do any results exist that suggest it cannot. It is, of course, possible that a crossover could occur between regimes I and II at Reynolds numbers higher than have been achieved in this work, although figure 8 suggests otherwise.

Significantly D_1 sits well above the other D_m and does not appear to converge with them during the most intense periods, which is why in figures 2, 3(*b*), 4(*b*) and 7(*b*) the D_m are plotted on a logarithmic scale with D_1 omitted. We are therefore justified in writing

$$\ln D_m \lesssim a_m \ln D_1 \quad \Rightarrow \quad D_m \lesssim D_1^{a_m}. \tag{5.1}$$

Plots of a_m for the first and second pair of simulations are shown in figure 9(*a*–*c*). Assuming a strong solution exists, the D_m have been shown to obey (see Gibbon 2012)

$$\dot{D}_m \leqslant D_m^3 \left\{ -\varpi_{1,m} \left(\frac{D_{m+1}}{D_m} \right)^{2m(4m+1)/3} + \varpi_{2,m} \right\}, \tag{5.2}$$

where the $c_{n,m}$ within $\varpi_{1,m} = \varpi_0 \alpha_m c_{1,m}^{-1}$ and $\varpi_{2,m} = \varpi_0 \alpha_m c_{2,m}$ are algebraically increasing with m. By dropping the negative term on the right-hand side of (5.2), and replacing the D_m^3 term with $D_m D_1^{2a_m}$ justified by (5.1), a time integration produces

$$D_m(t) \leqslant c_m \exp \int_0^t D_1^{2a_m} \,\mathrm{d}\tau \leqslant c_m \exp \left\{ t^{1-2a_m} \left(\int_0^t D_1 \,\mathrm{d}\tau \right)^{2a_m} \right\}, \quad 2a_m \leqslant 1. \quad (5.3)$$

Figure 9(*a–c*) show that while there is a weak dependence of a_m on both m and t, it nevertheless satisfies $2a_m < 1$ in all cases. Leray's energy inequality insists that $\int_0^t D_1 \,\mathrm{d}\tau < \infty$ so it is clear that the right-hand side of (5.3) is finite: *any* finite D_m is sufficient for Navier–Stokes regularity. This regularization can be traced to the *depletion of nonlinearity* in (5.1) in regime I. Although regime II has not been observed, (5.2) shows that it is associated with time decay of the D_m. Specifically, if $D_{m+1}/D_m \geqslant [c_{1,m}c_{2,m}]^{3/2m(4m+1)}$, then $\dot{D}_m < 0$ where $[c_{1,m}c_{2,m}]^{3/2m(4m+1)} \searrow 1$ for large m.

Acknowledgements

D.A.D. acknowledges the computing resources provided by the NSF-supported XSEDE and DOE INCITE programs under whose auspices some of these calculations were performed. R.P. and D.V. are members of the International Collaboration for Turbulence Research (ICTR). They acknowledge support from the 'Indo-French Center for Applied Mathematics', UMI IFCAM – Bangalore and, with RMK, the EU COST Action program MP0806 'Particles in Turbulence'. A.G. and R.P. thank DST, CSIR and UGC (India) and the SERC (IISC) for computational resources. J.D.G. and R.M.K. thank the Isaac Newton Institute, Cambridge, within whose programme *Topological Dynamics in the Physical and Biological Sciences (2012)* part of this work was carried out.

REFERENCES

Arneodo, A., Benzi, R., Berg, J., Biferale, L., Bodenschatz, E., Busse, A., Calzavarini, E., Castaing, B., Cencini, M., Chevillard, L., Fisher, R. T., Grauer, R., Homann, H., Lamb, D., Lanotte, A. S., Leveque, E., Luethi, B., Mann, J., Mordant, N., Mueller, W.-C., Ott, S., Ouellette, N. T., Pinton, J.-F., Pope, S. B., Roux, S. G., Toschi, F., Xu, H. & Yeung, P. K. 2008 Universal intermittent properties of particle trajectories in highly turbulent flows. *Phys. Rev. Lett.* **100**, 254504.

Betchov, R. 1956 An inequality concerning the production of vorticity in isotropic turbulence. *J. Fluid Mech.* **1**, 497–504.

Boffetta, G., Mazzino, A. & Vulpiani, A. 2008 Twenty-five years of multifractals in fully developed turbulence: a tribute to Giovanni Paladin. *J. Phys.* A: *Math. Theor.* **41**, 363001.

Bustamante, M. D. & Kerr, R. M. 2008 3D Euler about a 2D symmetry plane. *Physica* D **237**, 1912–1920.

Chakraborty, S., Frisch, U. & Ray, S. S. 2012 Nelkin scaling for the Burgers equation and the role of high-precision calculations. *Phys. Rev.* E **85**, 015301.

Doering, C. R. & Foias, C. 2002 Energy dissipation in body-forced turbulence. *J. Fluid Mech.* **467**, 289–306.

Doering, C. R & Gibbon, J. D. 1995 *Applied Analysis of the Navier–Stokes Equations*. Cambridge University Press.

Donzis, D., Sreenivasan, K. & Yeung, P. K. 2012 Some results on the Reynolds number scaling of pressure statistics in isotropic turbulence. *Physica* D **241**, 164–168.

Donzis, D. & Yeung, P. K. 2010 Resolution effects and scaling in numerical simulations of passive scalar mixing in turbulence. *Physica* D **239**, 1278–1287.

DONZIS, D., YEUNG, P. K. & SREENIVASAN, K. 2008 Dissipation and enstrophy in isotropic turbulence: scaling and resolution effects in direct numerical simulations. *Phys. Fluids* **20**, 045108.

ESWARAN, V. & POPE, S. B. 1988 An examination of forcing in direct numerical simulations of turbulence. *Comput. Fluids* **16**, 257–278.

FRISCH, U. 1995 *Turbulence: the Legacy of A. N. Kolmogorov*. Cambridge University Press.

GIBBON, J. D. 2010 Regularity and singularity in solutions of the three-dimensional Navier–Stokes equations. *Proc. R. Soc.* A **466**, 2587–2604.

GIBBON, J. D. 2011 A hierarchy of length scales for weak solutions of the three-dimensional Navier–Stokes equations. *Comm. Math. Sci.* **10**, 131–136.

GIBBON, J. D. 2012 Conditional regularity of solutions of the three-dimensional Navier–Stokes equations and implications for intermittency. *J. Math. Phys.* **53**, 115608.

GIBBON, J. D. 2013 Dynamics of scaled vorticity norms for the three-dimensional Navier–Stokes and Euler equations. *Procedia IUTAM: Proceedings of IUTAM Symposium Topological Fluid Dynamics II*, vol. 7, pp 39–48.

HENTSCHEL, H. G. E. & PROCACCIA, I. 1983 The infinite number of generalized dimensions of fractals and strange attractors. *Physica* D **8**, 435–444.

HOLM, D. D. & KERR, R. M. 2007 Helicity in the formation of turbulence. *Phys. Fluids* **19**, 025101.

ISHIHARA, T., GOTOH, T. & KANEDA, Y. 2009 Study of high-Reynolds number isotropic turbulence by direct numerical simulation. *Annu. Rev. Fluid Mech.* **41**, 16–180.

JIMENEZ, J., WRAY, A., SAFFMAN, P. G. & ROGALLO, R. S. 1993 The structure of intense vorticity in isotropic turbulence. *J. Fluid Mech.* **255**, 65–90.

KERR, R. M. 1985 Higher-order derivative correlations and the alignment of small-scale structures in isotropic numerical turbulence. *J. Fluid Mech.* **153**, 31–58.

KERR, R. M. 1993 Evidence for a singularity of the three-dimensional incompressible Euler equations. *Phys. Fluids* A **5**, 1725–1746.

KERR, R. M. 2011 Vortex stretching as a mechanism for quantum kinetic energy decay. *Phys. Rev. Lett.* **106**, 224501.

KERR, R. M. 2012 Dissipation and enstrophy statistics in turbulence: are the simulations and mathematics converging? *J. Fluid Mech.* **700**, 1–4.

KERR, R. M. 2013 Bounds on a singular attractor in Euler using vorticity moments. *Procedia IUTAM, Proceedings of IUTAM Symposium Topological Fluid Dynamics II*, vol 7, pp. 49–58.

KERR, R. M. 2013*a* Swirling, turbulent vortex rings formed from a chain reaction of reconnection events. *Phys. Fluids* **25**, 065101.

KERR, R. M. 2013*b* Bounds for Euler from vorticity moments and line divergence. *J. Fluid Mech.* (in press).

MENEVEAU, C. & SREENIVASAN, K. R. 1991 The multifractal nature of turbulent energy dissipation. *J. Fluid Mech.* **224**, 429–484.

MENEVEAU, C., SREENIVASAN, K. R., KAILASNATH, P. & FAN, M. S. 1990 Joint multifractal measures: theory and applications to turbulence. *Phys. Rev.* A **41**, 894–913.

NELKIN, M. 1990 Multifractal scaling of velocity derivatives in turbulence. *Phys. Rev.* A **42**, 7226–7229.

ORSZAG, S. A. & PATTERSON, G. S. 1972 Numerical simulation of three-dimensional homogeneous isotropic turbulence. *Phys. Rev. Lett.* **28**, 76–79.

PANDIT, R., PERLEKAR, P. & RAY, S. S. 2009 Statistical properties of turbulence: an overview. *Pramana – Journal of Physics* **73**, 157–191.

RAY, S. S., MITRA, D. & PANDIT, R. 2008 The universality of dynamic multiscaling in homogeneous, isotropic Navier–Stokes and passive-scalar turbulence. *New J. Phys.* **10**, 033003.

RAY, S. S., MITRA, D., PERLEKAR, P. & PANDIT, R. 2011 Dynamic multiscaling in two-dimensional fluid turbulence. *Phys. Rev. Lett.* **107**, 184503.

ROGALLO, R. S. 1981 Numerical experiments in homogeneous turbulence. *Tech. Mem.* 81835. NASA.

SAHOO, G., PERLEKAR, P. & PANDIT, R. 2011 Systematics of the magnetic-Prandtl-number dependence of homogeneous, isotropic magnetohydrodynamic turbulence. *New J. Phys.* **13**, 013036.

SCHUMACHER, J., SREENIVASAN, K. R. & YAKHOT, V. 2007 Asymptotic exponents from low-Reynolds-number flows. *New J. Phys.* **9**, 89–107.

SREENIVASAN, K. R. 1985 On the fine-scale intermittency of turbulence. *J. Fluid Mech.* **151**, 81–103.

YAKHOT, V. & SREENIVASAN, K. R. 2004 Towards a dynamical theory of multifractals in turbulence. *Physica* A **343**, 147–155.

YEUNG, P. K., DONZIS, D. & SREENIVASAN, K. R. 2012 Dissipation, enstrophy and pressure statistics in turbulence simulations at high Reynolds numbers. *J. Fluid Mech.* **700**, 5–15.